INTERNSHIP REPORT

Analysis of Giant Unilamellar Vesicles

from droplet to vesicle

Supervisors:
dr. K.A. (Kristina) Ganzinger (AMOLF)
dr. G.A. (Gerhard) Blab (Utrecht University)

PHYSICS OF CELLULAR INTERACTIONS
Living Matter Department
AMOLF

L.D. (Roy) Hoitink BSc

July 24, 2020

Abstract

In bottom-up reconstitution, a minimal cell is crafted from only essential components. Lipid vesicles are often used in this approach to mimic a cell's membrane due to their structural resemblance. Most prominently giant unilamellar vesicles (GUVs), which are lipid vesicles with a single lipid bilayer and a size in the range of 1-100 μm, are used in this field. Although there are several methods for producing these GUVs, the cross droplet interface crossing encapsulation (cDICE) is the most robust method, even though it being invented only several years ago. To further improve the reliability of this method and allow for easier troubleshooting, two tools were created. The first tool, an imaging setup that should image emulsion droplets of the cDICE setup at high speed, was able to use both epi- and trans-illumination for the imaging of static emulsion droplets in a model system. The used exposure times are already on the μs-timescale, which is probably sufficient for application on the cDICE setup. Difficulties in alignment of the imaging setup on the cDICE-setup, due to the lack of fine translation, lead to the fact that the setup was not yet successfully employed on the cDICE-setup. The second tool, which performs an analysis on the positions and sizes of GUVs from confocal microscopy data, has proven to track the vesicles generally well. In higher-density samples some problems arise, such as the false detection of aggregates, but these can easily be solved by manual inspection from the user. In the end the data analysis tool is ready to use and allows for easier analysis of the parameter space of the cDICE, but the second tool still needs some adaptions, for example an implementation of trans-illumination in the cDICE and a manner for finer adjustment of the alignment.

Contents

Chapter 1

Introduction

The human body is made up of numerous cells, each having their own function but working together closely to ensure the body survives. In order to better understand the processes within and among cells, there are two main approaches that allow for simplification and easier understanding of cells, the bottom-up reconstitution and top-down approach. In the bottom-up reconstitution approach one uses only the minimal amount of components required for a functioning system, which means that we are working with systems that model the behaviour of cells. For example, if one wants to study the process of phagocytosis, in which the cell can uptake particles or even other cells from its environment, one could aim to build a minimal system to which only proteins and other building blocks that directly take part in the process are added [1]. In contrast, the top-down approach starts with fully functional cells and removes unwanted elements until only the necessary components remain. Ideally, both the top-down and bottom-up approach would reach the same end state, but in fact most top-down studies only look at the effect of removing one or few components from the complex system, still leaving undesired and unforeseen cross-talk effects, where different processes influence each other, in place. As in the bottom-up approach no extra processes should be present, this is not the case for the bottom-up approach [2].

1.1 Liposomes

Often there is the desire to mimic the cell's membrane in such model systems, in order to separate internal from external compartments and to work with a more or less closed system that is finite in resources. A widely used approach is the use of lipid vesicles, or liposomes, which are vesicles comprised of at least one bilayer of lipids [3]. These lipids are amphiphilic, indicating they have both hydrophilic and hydrophobic parts. The head group of these lipids, a phosphate group in the generally used phospholipids, is hydophilic and therefore has a preference to be placed in an aqueous environment, while its hydrophobic tail rather resides in oily (apolar) environments. Their amphiphilic nature makes these phospholipds are excellent at stabilising emulsions, as the lipids will position themselves spontaneously at the droplets' interfaces. Next to stabilising emulsions, these lipids can also form bilayers in which the hydrophobic tails are oriented towards each other, leaving the hydrophilic head groups pointing outwards. These bilayers can then form the boundary between two different aqueous environments, as illustrated in Fig. 1.2a. [3]

The existence of bilayers within a liposome leads to formation of separate containers, all shielded by their own membrane, as shown in Fig. 1.2b. Liposomes with multiple bilayers are called multilamellar, as opposed to unilamellar bilayers that have only a single bilayer. Within the field of synthetic biology giant unilamellar vesicles (GUVs), which are unilamellar liposomes with diameters ranging from 1 μm to 100 μm, are most often used as they are in the same size regime as cells and do create a bounded environment for the vesicle's contents [2, 4–6]. A large benefit of using GUVs as model systems, rather than surface based membranes, is their ability to provide the same boundary conditions as cells do, only substances that can diffuse over a cell's membrane will be able to pass the liposome's membrane. [2].

1.2 Synthesis of Giant Unilamellar Vesicles (GUVs)

As a giant unilamellar vesicle with only one closed bilayer is not the thermodynamically most stable state, but rather at a kinetically trapped state, care must be taken into the preparation of GUVs, to prevent the formation of multilamellar structures [7]. This was already noted by Reeves

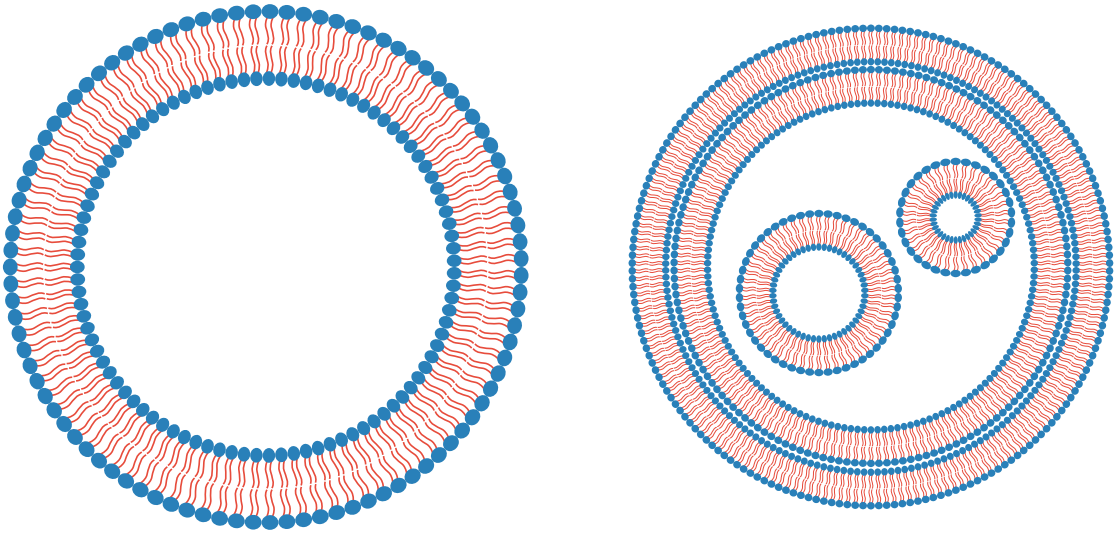

(a) (b)

Figure 1.1: Two examples of liposomes. **(a)** Unilamellar liposome with only a single bilayer and **(b)** a mulitlamellar liposome with multiple bilayers, each bilayer makes its own compartment.

and Dowben, when they proposed the first method to form GUVs in 1969 [8]. Their method is based on the swelling of a lipid film that was dried onto a glass surface. They noted that slight disturbing or agitation of the solution lead to formation of vesicles with multiple bilayers, which is mostly undesired [8].

The mechanism behind electroformation of GUVs is based on the same principle as was invented by Reeves and Dowben [7, 9, 10]. The lipids are now spread on an electrode and application of an electric field gives better control over the hydration process and therefore leads to a higher yield of GUVs.

Another class of GUV formation techniques is based on emulsions. As the inside of a GUV is usually an aqueous mixture, it is best to start from a water-in-oil (w/o) emulsion. Most ideally, one would want to use a lipid stabilised w/o emulsion, with lipids that can form a bilayer. The hydrophilic head groups of the lipids are positioned inside the water droplets, while the hydrophobic tails are pointing outwards into the apolar phase. Upon (forced) crossing of the interface between the oil and water phase - which will also be saturated with lipids - the vesicle obtains the second layer of lipids, forming the bilayer, as illustrated in Fig. 1.2.

This mechanism is exploited in the cDICE method, which is an acronym for **c**ontinuous **d**roplet **i**nterface **c**rossing **e**ncapsulation [11]. In this method the oil with lipids and aqueous buffer are placed in a rotating chamber. The density of the aqueous phase needs to be higher, to make sure that will be at the outside of the chamber. The droplets are formed by placing a capillary into the oil layer and droplets are sheared off and forced through the interface because of the centrifugal force acting upon them. [11] Within AMOLF a custom cDICE-setup was developed, as shown in Fig. 1.3. A capillary, attached to a syringe pump, can be inserted into the setup and placed in the chamber (Fig. 1.3b). Rotation speeds can easily be configured on the device itself and flow speeds are controlled via an external syringe pump.

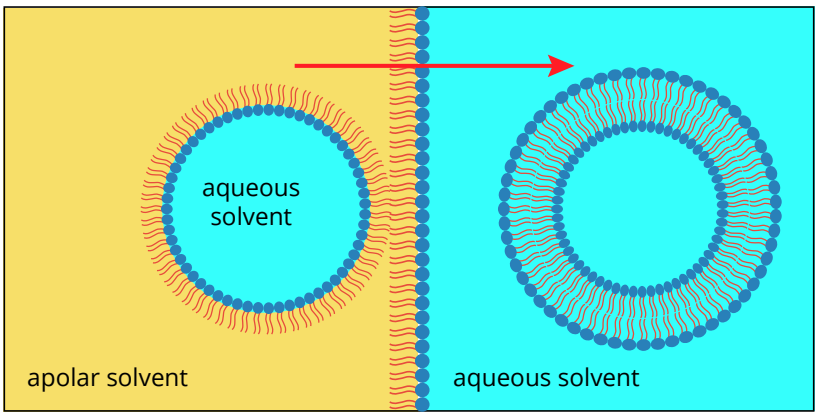

Figure 1.2: Formation of a GUV from a lipid-stabilised water-in-oil emulsion by passing to a fluid-fluid interface. Upon crossing the interface, the vesicle obtains its second lipid layer, completing the bilayer.

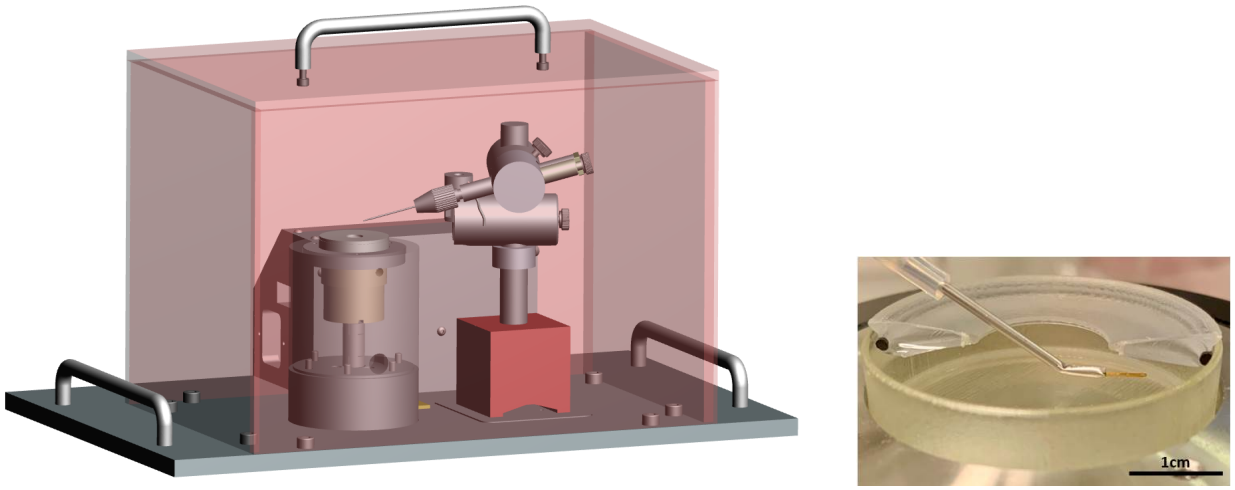

(a) **(b)**

Figure 1.3: The custom cDICE-setup developed within AMOLF, **(a)** shows a CAD drawing of the setup (without syringe pump) and **(b)** the rotating chamber with lid sliced in half for viewing purposes.

1.3 Analysis of GUVs

Once the vesicles are formed, they are generally dispersed in an aqueous medium. The vesicles then need to be analysed in order to characterise their properties, e.g. what their sizes, shapes and membrane properties are. A widely used analysis method for liposomes is confocal microscopy, as (part of) the lipid molecules can be exchanged for their fluorescently labelled analogues. The fluid nature of the lipid bilayer allows for the fluorescent molecules to diffuse over all of the membrane, making the whole vesicle fluorescent [12].

Confocal microscopy is a type of fluorescence microscopy, in which a laser is scanned along a sample in order to excite a fluorophore, that absorbs photons from the laser, to a higher energy state [13, 14]. After excitation, the excited state of the fluorophore will spontaneously return to its ground state in a radiative manner, again emitting photons. As often some energy is lost on the form of non-radiative decay (i.e. vibrational transitions), the energy of the emitted photons is typically lower than the photons used for excitation, resulting in light of a longer wavelength. This so called Stokes shift, makes that the excitation and emission photons can be optically separated and the emitted signal can be detected onto a detector. The special feature of confocal microscopy is the addition of a so called pinhole, which is able to reject out of focus light. Part of a setup of a

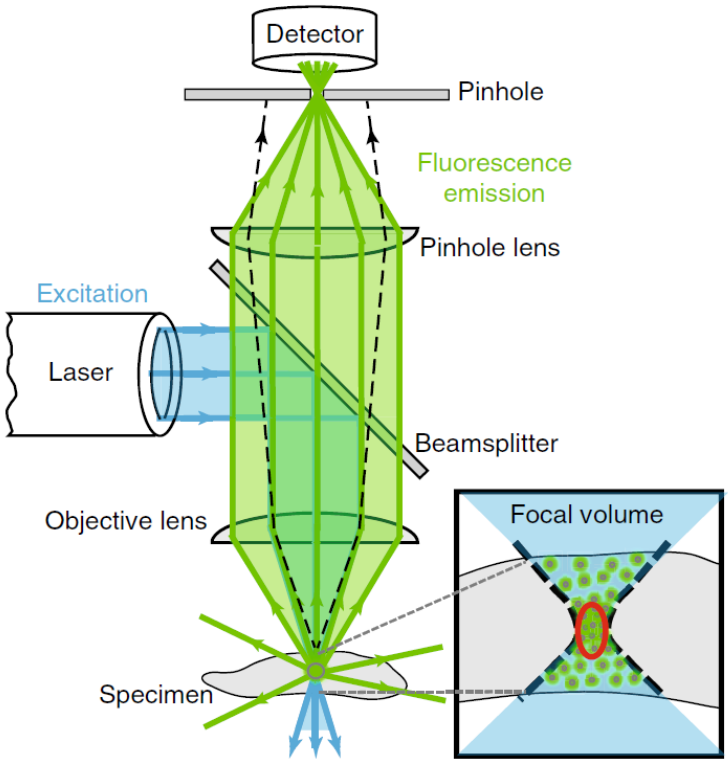

Figure 1.4: Principle of confocal microscopy. A laser is used to excite the fluorescent molecules, after which the out-of-focus fluorescent signal is discarded by the pinhole, such that only light from a small focal volume reaches the detector. Source: Fig. 2a from ref. [13].

confocal microscope is schematically illustrated in Fig. 1.4. By moving the sample (or objective), and thus the distance from the pinhole, a different imaging plane can be brought into focus. By stacking these planes, a 3D image is obtained of the liposomes. The addition of the pinhole allows for resulting resolutions on the order of 200 nm in lateral and 500 nm in axial direction , far smaller than the typical size of our GUVs, making it a suitable technique. Several super-resolution methods such as stimulated emission depletion (STED) and Stochastic optical reconstruction microscopy (STORM) exist to even further increase the resolution, but these high-resolution techniques are not necessary for our purpose as we are dealing with length scales in the tens of microns. [13, 14]

Using confocal microscopy, we can image the morphology of the GUV as a whole. For example, we can extract their shape and diameter. Other methods are available to obtain a more detailed understanding of the bilayer, such as fluorescence recovery after photobleaching (FRAP) to investigate the lipid fluidity or fluorescence correlation spectroscopy (FCS) for assessment of membrane protein association [12]. As these techniques lie beyond the scope of this thesis, they will not be further elaborated on.

1.4 Scope of this Thesis

Since synthesis of liposomes, and more specifically, lipid vesicles with specified properties such as a predefined size and lamellarity is still a relatively new field, we want to shed light on the production process as a whole. We do this by making tools to look at the very start, the formation of droplets with cDICE as well as the very end, at which the synthesised GUVs are analysed by confocal microscopy.

This report describes the process of developing two tools for improving lipid vesicle formation. In Chapter 2, the process of a building simple microscope for imaging high speed droplets is described, to shed light on the morphology of emulsion droplets produced by the cDICE method. Given that droplet morphology could influence the quality, size and polydispersity of the syn-

thesised GUVs, knowing more about droplet morphology allows to draw relationships between these two states in GUV formation. Even though we did not succeed in imaging droplets within the cDICE, most likely the spatial and temporal resolution required have been reached with the designed setup.

Chapter 3 will then focus on a data analysis tool for the confocal microscopy data of GUVs. This tool assists the user in obtaining statistics on a GUV synthesis run, allowing for easier and faster comparison between runs, which facilitates faster scanning of the parameter space and comparison therein. The tool was build successfully and was in general capable of performing accurate tracking and size estimation of the produced vesicles, only minor problems arise when aggregates are formed within samples.

The report is concluded with Chapter 4 in which some general conclusions are drawn and an outlook is given.

Chapter 2

Towards High Speed Imaging of Emulsion Droplets

2.1 Introduction

Optical microscopes have been of great assistance to science. The main goal is to act as a magnifier, allowing the user to see object smaller than can be see with the naked eye. To shed light on the morphology of the emulsion droplets formed with the cDICE method (Section 1.2), we aim to build a simple microscope with a camera attached to take snapshots of the droplets.

2.1.1 Microscope Requirements

As the cDICE produces microscopic droplets at high speed, it is important that our microscope has sufficient resolution in both space, to be able to see the shape of the droplets, and time, to quickly take snapshots of individual droplets. The cDICE method has a flowrate of typically $25\,\mu l\,min^{-1}$ and we assume a typical droplet radius of $5\,\mu m$. This means our spatial resolution should be able to visualise droplets of $10\,\mu m$ in diameter. The goal is to look at the droplet morphology, we would ideally want at least 10 px for the diameter of a droplet, which would mean that our pixel size should be equal to or smaller than $1\,\mu m\,px^{-1}$.

Our temporal resolution is limited by the flowrate of the cDICE setup, assuming the most favourable scenario in terms of yield, all of the streaming fluid is converted into a droplet. If this is the case, it takes ~1.26 μs to form a single droplet and the droplet forming rate is therefore on the order of 793 650 Hz. The illumination time should ideally be on the order of 1 μs to prevent motion blur.

Illumination methods

We need to establish an image of the sample onto the sensor of the camera by illuminating the sample. We can illuminate the sample in several ways, but most commonly used are epi- and trans-illumination [15]. With trans-illumination light is directed through the sample, as schematically illustrated in Fig. 2.1a. This method is naturally limited by both the transparency of the sample and the contrast difference between species to image and the background in the sample. The emulsions that are used are all transparent, so the transparency of the sample does not form a problem. However, as the cDICE method makes use of a rotating metal plate, illumination from below the chamber is difficult as the power source for the light either needs to be integrated, making the chamber higher, or the cable from power source to light needs to cope with the rotations without being twisted together.

The epi-illumination is a better choice if the back of the sample is unreachable, as the light source can be placed perpendicular to the optical axis, as shown in Fig. 2.1b. The light is directed onto a beamsplitter, that transmits 50% of the light and reflects the other half into the objective. The objective then foucuses the light beam into the focal spot in the sample, from which part of the light is reflected back into the objective, towards the lens and camera sensor. Again, upon passing the beamsplitter half of the light is lost. The disadvantage of epi-illumination is the loss of light, as the light passes twice through a beamsplitter, each time losing 50% of its intensity, ending up with only 25% reaching the sensor. Furthermore, with epi-illumination the illumination is more shallow, as the light no longer proceeds through the whole sample but is rather focused into a small region and then reflected back.

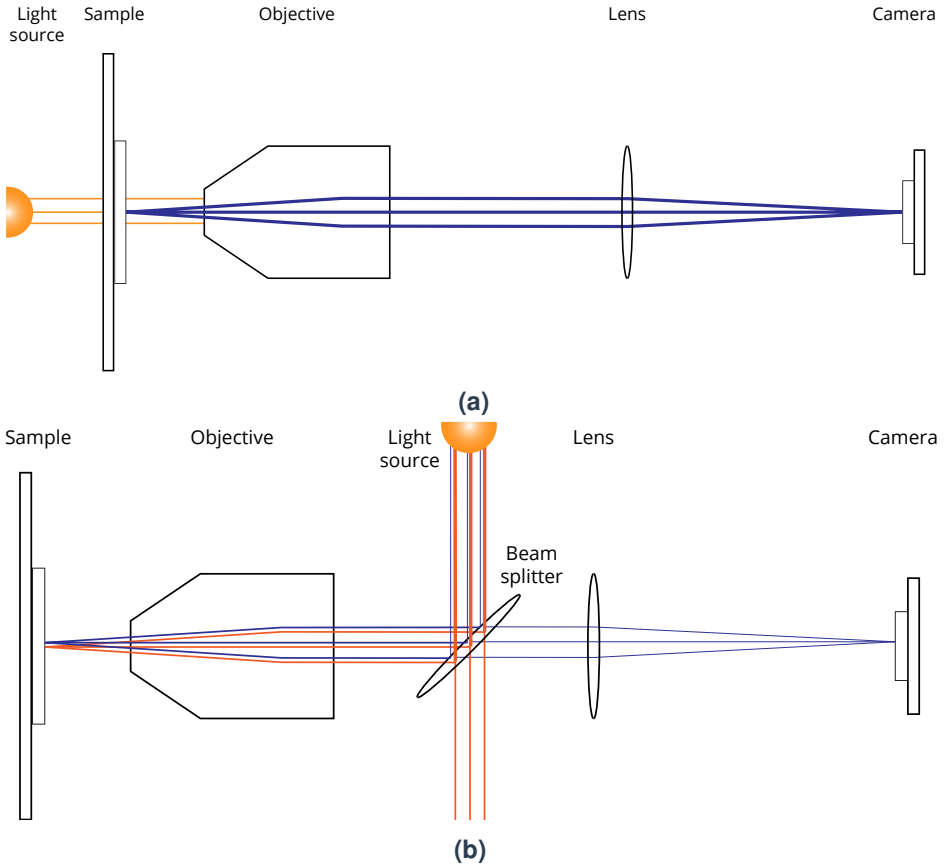

Figure 2.1: Schematic illustration of a **(a)** trans-illumination and **(b)** epi-illumination setup. Orange lines depict light directly from the light source, while the blue lines indicate light transmitted through (in **(a)**) or reflected by (in **(b)**) the sample.

2.1.2 High-Speed Imaging

When using a continuous light source, either in trans- or epi-illumination mode, the camera is the limiting factor in terms of imaging speed. While most modern CCD (video)cameras are easily capable of recording videos at 30-60 frames per second (fps), this still indicates an exposure time of 16.7 µs at the fastest available framerate [16]. Considering the formation time of one droplet in the cDICE setup is on the order of 1.26 µs, this framerate will not suffice to resolve individual droplets. If the displacement of a droplet is too high, the recorded picture will be subject to motion blur, causing the image to become hazy in the direction of displacement [17]. This is a well-known problem in high-speed imaging on both the micro- and macroscopic scale, an example on microscopic scale is given in Fig. 2.2.

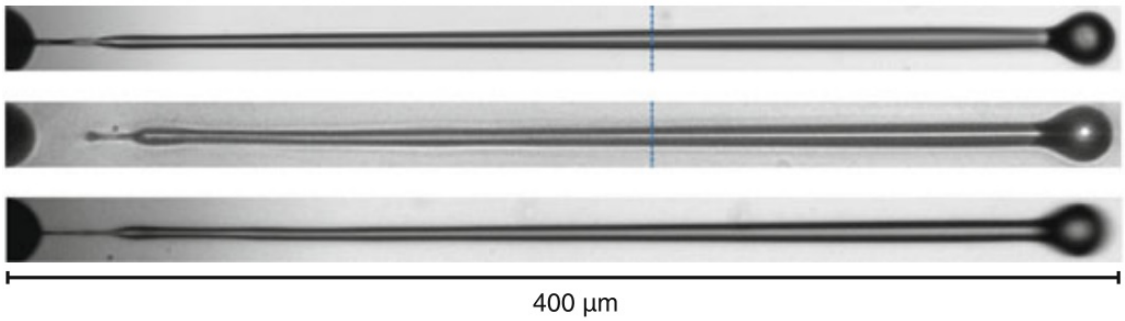

Figure 2.2: Illustration of motion blur in the bottom row. The droplets looks sharp in the first rows, but due to longer illumination time in the bottom row, motion blur occurs. Adapted from Fig. 8 in ref. [17].

There are commercial high-speed cameras available that can easily go above 10 000 fps, but their speed comes with a very high price [16]. The high price of these cameras is outside the budget available and the goal is to find a solution that works good for a descent price, such that other solutions need to be considered.

The motion blur problem could also be resolved by using a pulsed rather than continuous light source. The length of the light pulses can easily be shorter than the 16.7 μs that would be reached at 60 fps, but the energy of the light pulse needs to be sufficiently high to be able to expose the sensor enough on the short timescale. The most notorious example of a pulsed high-intensity light source is a laser, that can deliver pulses in the femtosecond-range, but drawbacks of using laser-based illumination originate from the coherent nature of the laser light. The long coherence length results in diffraction fringes and laser speckle patterns in the images recorded [18]. A solution to this problem was proposed by van der Bos et al. [17]. They report a setup that places a total internal reflection lens, filled with a laser dye solvent, in front of the coherent light beam, decreasing its coherence as the laser light is absorbed by the dye, re-emitted and reflected onto the sample [17]. While this setup has been proven to work, the incorporation of a dye filled lens together with a laser will complicate the setup and involve high costs, making it unsuitable for our purpose.

As light emitting diodes (LEDs) are known to have very high switching speeds and can therefore provide pulses in the nanosecond range, they are very plausible candidates for a pulsed illumination source [19]. LEDs contain a semiconductor, in which electrons are excited from the valence to the conduction band upon passing a current through. Light is subsequently emitted from the semiconductor, upon radiactive decay of the electrons. The colour of the light emitted by the LED is dependent on the height of the band gap, the distance between valence and conduction band, and therefore the semiconductor material that is used. An LED can easily be switched on and off by passing a current through, if the current is present, the LED is on, else it is off. If we therefore generate a pulsed current of an amperage suitable for the chosen LED and a pulse length with the illumination time that we want, we have a strong, pulsed, non-coherent light source that can be used for illumination.

Being cheap and also able to provide high switching times, the LED is the best candidate for the low-cost imaging setup for taking snapshots of emulsion droplets in the cDICE setup. Ideally, this would be combined with epi-illumination, as trans-illumination is difficult with the rotating metal plate.

2.2 Materials and Methods

2.2.1 Preparation of the Model System

To test the imaging, a model system was used with droplets on the same order of diameter as produced by the cDICE method. This model emulsion was produced by adding 250 µl lipid-in-oil solution (0.2 mg mL^{-1} lipids (99.9 mol% DOPC, 0.1 mol% ATTO655 DOPE) in solution of 75.2% silicon oil, 18.8% mineral oil and 6% chloroform) and then 5 µl aquaeous buffer (composition: 600 mOsm glucose in MilliQ (158.15 µl), MilliQ water (249.75 µl), and OptiPrep (92.1 µl)) to a 500 µl Eppendorf tube. This emulsion was then rubbed over a Microcentrifuge Tube Rack (5x16 holes) in length direction to mix the solution and form droplets, upon which the solution went from clear to hazy. After emulsification, the emulsion was then loaded into a hollow rectangular borosilicate capillary (Vitrocom, inner diameter 0.30 mm × 3.00 mm). The capillary was placed onto a #5 microscopy slide (Menzel-Gläser, 24 mm × 60 mm) and ends were fixed with two-component epoxy glue (Bison), afterwards the glue was dried to air for several hours. The model system could then be fixed onto a 30 mm optical cage (Thorlabs), that allowed mounting in the setup (as shown in Fig. 2.3).

Figure 2.3: Attachment of the capillary containing the emulsion to an optical cage.

2.2.2 Imaging Setup

To keep the imaging solution low-cost a Raspberry Pi mini computer (model 3B) was used together with a Raspberry Pi camera (V2). The Raspberry Pi was connected to a 7″ touch screen (Raspberry Pi), that displays a small user interface via a webpage to allow viewing and capturing of the camera's images. A custom LED driver was designed that could be mounted on top of the Raspberry Pi and be powered directly through the Pi's GPIO (general-purpose input/output) pins. This LED driver is capable of of delivering a pulsed current at 1 A with pulse lengths that can be of any length, tuned in steps of 2.5 µs. After each pulse a short delay period is implemented, which is also customisable in steps of 2.5 µs, in which no current is delivered to the connected LED.

For mounting and alignment of the optical setup, a standard 30 mm optical cage system (Thorlabs) was used. For the measurements with an objective, a Nikon Plan Fluor 4x/0.13 PhL DL objective was used.

2.3 Results and Discussion

2.3.1 Regular Camera Lens, without Objective

The Raspberry Pi camera itself as pixel size of 1.12 µm × 1.12 µm [20], which is close to the pixel size that we need, so the first attempt of imaging droplets was without any further magnification. The standard camera lens was used. The microscopy slide was raised from the table to minimise background by placing it onto two plastic caps. The camera was then mounted about 3 cm above the sample and a continuous light source (phone camera flash light) was used for illumination from above, the setup is schematically illustrated in Fig. 2.4a.

In Fig. 2.5 the results from imaging with only the default camera lens without objective are shown. The emulsion in Fig. 2.5a was rubbed along the tube rack for 12 times, causing very small droplets,

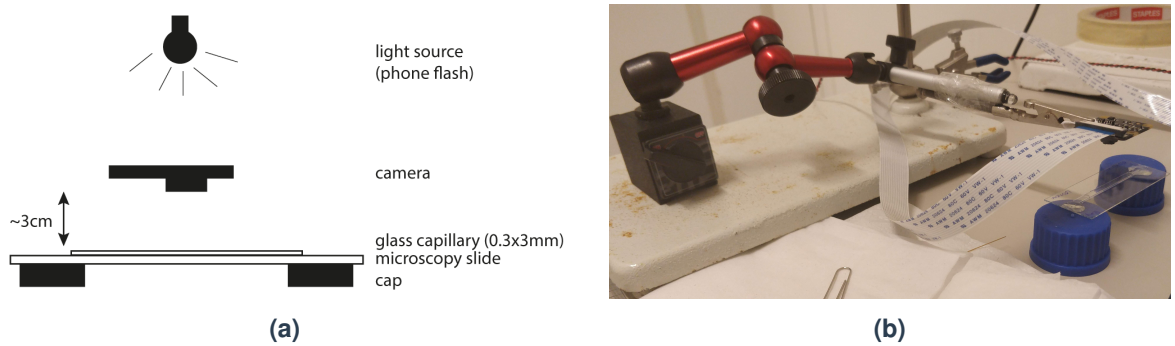

Figure 2.4: Setup used for imaging without objective, **(a)** shows a schematic illustration and **(b)** shows a picture of the setup (light source not shown).

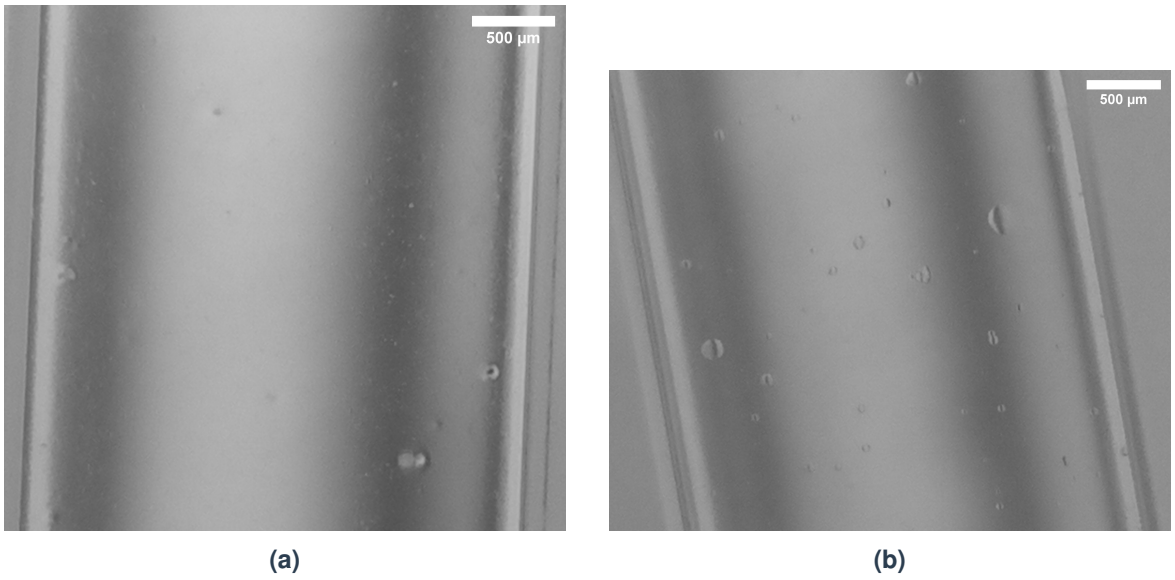

Figure 2.5: Images of two different emulsions with the raspberry pi camera without an objective.

while the emulsion in Fig. 2.5b was rubbed along for 7 times, giving better visible droplets. The scale in both images was estimated using the width of the capillary (ID 3.00 µm), resulting in a scale of 0.78 px µm^{-1} (equivalent to 1.3 µm px^{-1}). Large droplets are easily distinguishable from the background, up to droplets of ~30 µm in diameter could still be viewed at a 100% magnification.

Another matter that is clear from the images is the shadows that are cast behind the capillary, in Fig. 2.5 displayed as dark lines along the inner borders of the capillary. These shadows because epi-illumination is used combined with a very bright light source, placing the capillary further away from the (white) table would already diffuse the shadow more, minimising their appearance and disturbance to the contrast of the sample.

2.3.2 Imaging through 4x objective

To increase resolution, a 4x objective (Nikon Plan Fluor 4x/0.13 PhL DL) was added to the setup, and the standard pi camera lens was replaced by a 200 mm focal length achromatic lens (Thorlabs AC254-200-A-ML). The whole structure was mounted in an optical cages setup to allow for easier alignment, as shown in Fig. 2.6. The setup was aligned such that a sharp image was produced on the sensor, judged by looking at the output of the camera on the screen. To shield the setup from stray light, as cardboard box was placed over the setup, preventing unwanted light from entering the lens and/or camera sensor.

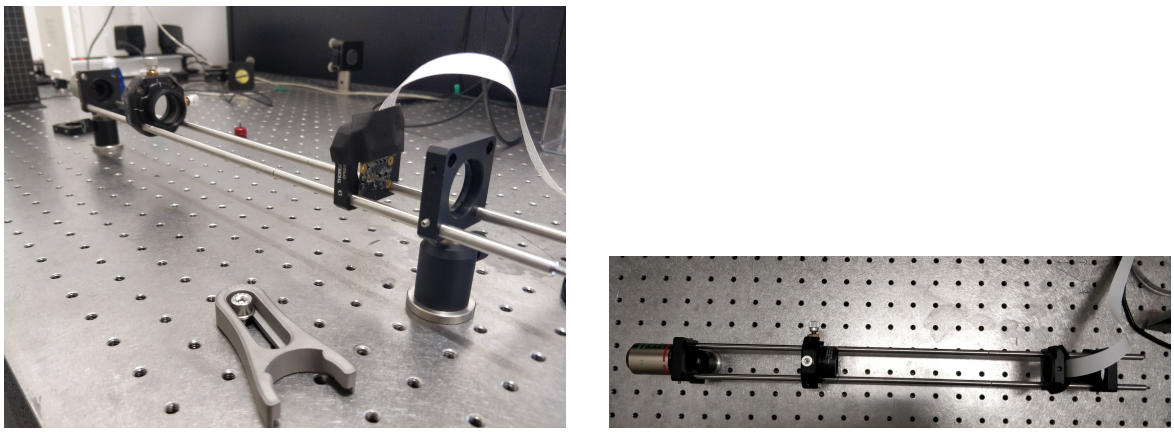

(a) (b)

Figure 2.6: Imaging setup in optical cage system

2.3.3 Trans-illumination with a Continuous Light Source

An LED mini-light (Thorlabs PSX501) was used as a continuous illumination source to provide diffuse white light. The flexible arm of the mini-light allowed for easy rotation and twisting for alignment of the light with respect to the sample.

Figure 2.7: Setup used for trans-illumination with a continuous light source.

The setup that was used is depicted in Fig. 2.7. The light can easily be oriented and twisted to provide trans-illumination as shown in the figure, the light is placed behind the sample and the transmitted light goes into the objective, through the lens focused on the camera's sensor. As we are working with a colour camera, it captures an RGB image, containing three channels for red, green and blue light respectively. The channels are combined into one image, as shown in Fig. 2.8a. The RGB image can be converted to grayscale (Fig. 2.8b) by taking a weighted average with weights 29.9%, 58.7% and 11.4% for the R, G and B channel respectively, as is compliant with the commonly used ITU-R 601-2 luma transform. The relatively large weight for the green channel is chosen since our eyes are also most sensitive to green and this will therefore be the most accurate representation. Since the image quality does not degrade by conversion but the fewer colours make them less distracting, all images in this chapter are converted to grayscale using the aforementioned method.

When we split the image into different channels, as is shown in Fig. 2.8c-e, we see that there is a slight difference in contrast and brightness between each of them, but none of them is notably better than the combined image.

The scale in the previous images was determined using a microruler (Pyser-Sgi S8), from which a

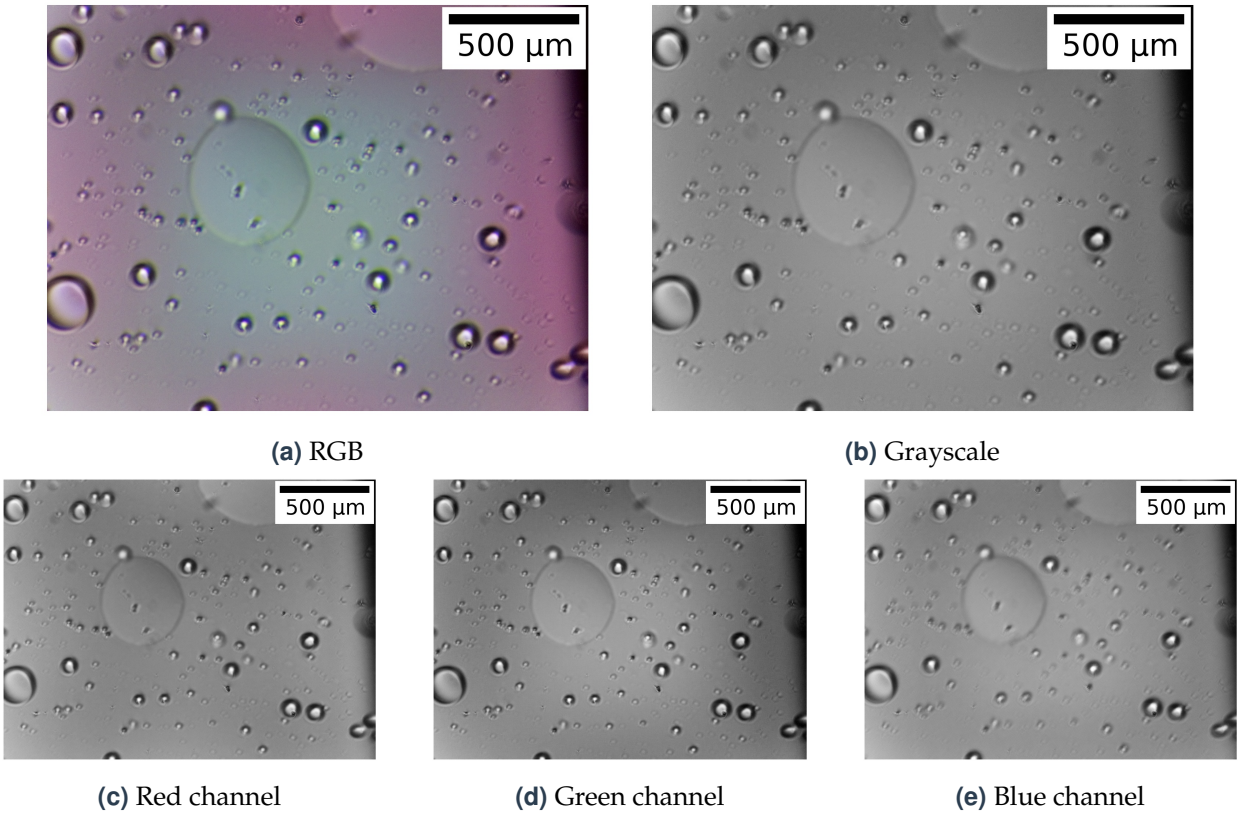

(a) RGB **(b)** Grayscale

(c) Red channel **(d)** Green channel **(e)** Blue channel

Figure 2.8: Caption

pixel size of 1.58 px µm^{-1} (or equivalently 0.633 µm px^{-1}).

2.3.4 Trans-illumination with Pulsed Light-Source

The continuous LED light source was exchanged for a pulsed LED light source. Two types of pulsed light sources were tested, i) an array of three 4000 K 500 mW LEDs (Cree JE2835BWT-P-H40GA0000-N0000001, 76 lm@150 mA) and ii) a single high-power 4000 K LED (Luxeon V2, 315 lm@700 mA). All LEDs were powered by a 1 A pulsed current and pulse times could be varied in steps of 2.5 µs. Both LEDs are displayed in Fig. 2.9.

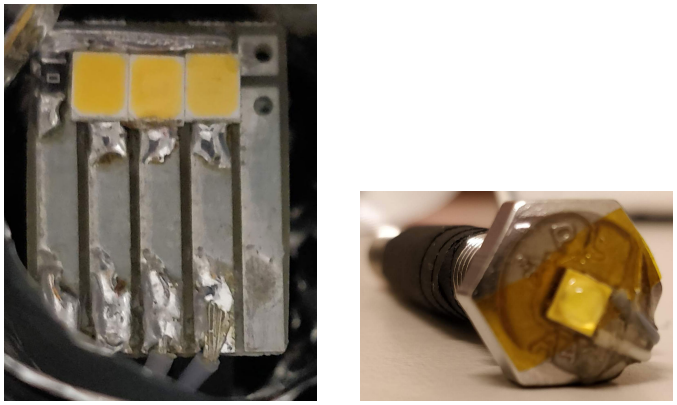

(a) **(b)**

Figure 2.9: Images of **(a)** the triple LED array and **(b)** the single high-power LED.

Results of varying the illumination times for 25 µs, 10 µs and 2.5 µs with the triple LED array are given in Fig. 2.10. It is immediately clear from the image that decreasing the exposure time, also

decreases the signal-to-noise ratio. As the contrast and brightness of all images were normalised for display purposes, we can see that the images for shorter exposure times become darker and more grainy. It becomes harder to see the smaller droplets, but large droplets are still very easy to distinguish. But still at only 2.5 µs exposure (Fig. 2.10c) the overall shape of the droplets is clearly visible, and illumination with a brighter pulsed light source for the same exposure time would improve the image and therefore be sufficient for our purpose.

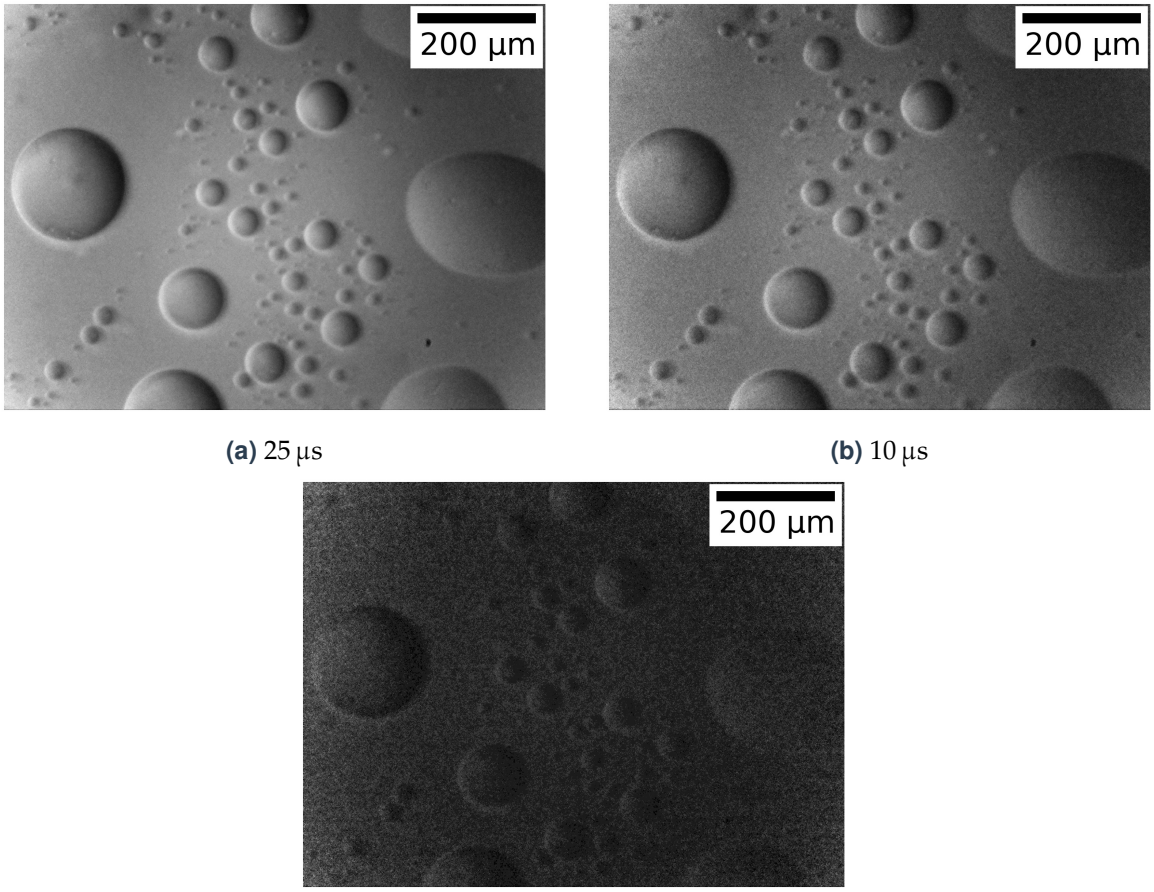

(a) 25 µs **(b)** 10 µs

(c) 2.5 µs

Figure 2.10: Influence of different illumination times with the triple LED array on the quality of the images, illumination time is given for each of the subfigures.

We can clearly see the decrease of signal when looking at the pixel intensity distributions in Fig. 2.11. As we are dealing with 8-bit images, the maximum value a pixel can obtain is 255 ($= 2^8 - 1$). A pixel with value 255 would be completely white, opposed to a pixel with value 0 being completely black in these grayscale images. Even at longest exposure time (25 µs, Fig. 2.11a), the maximum pixel value is still below 80. We see that for decreasing exposure time the pixel intensity distribution rapidly shifts to lower values, but the relative spread of the distribution, standard deviation divided by the mean intensity, increases. This indicates that as brightness decreases, shown by the decrease of the mean intensity, the contrast decreases less fast, since contrast is linked to the width of the distribution [21].

Fig. 2.12a displays an image taken with the single high-power LED at 25 µs exposure time. This specific sample contains less droplets, but the contrast is till good. The intensity histogram in Fig. 2.12b shows a much higher value than we saw previously in Fig. 2.11, but this is mainly caused by the large presence of background signal in this specific sample. As trans-illumination was used, any spot that does not contain droplets, and therefore only transparent oil, will just transmit the light, increasing the overall brightness of the image. This makes clear that intensity histograms can only be compared among images of exactly the same sample, with the exact same

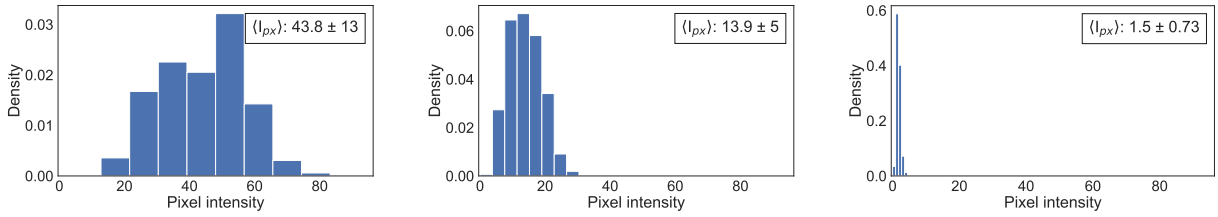

(a) 25 µs **(b)** 10 µs **(c)** 2.5 µs

Figure 2.11: Pixel intensity distributions for trans-illumination with the triple LED array at different exposure times. The inset displays the mean pixel value together with the standard deviation.

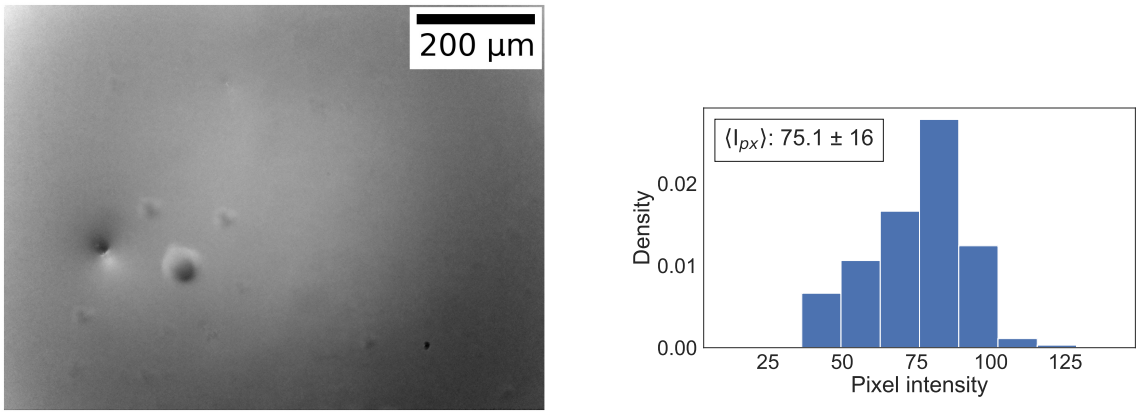

(a) **(b)**

Figure 2.12: Trans-illumination with the single high-power LED at 25 µs exposure time. **(a)** shows the image itself and **(b)** the distribution of pixel intensities.

illumination position where only the exposure time is varied. This problem is hard to overcome, usually such issues would be resolved by taking a reference image with a baseline sample (only oil, no droplets in this case) and the exposure set to a fixed value. This baseline image can then be subtracted from each image taken in order to more realistically compare among samples. As alignment is done by hand and the different LEDs are placed in roughly the same position, which means that position vary if the LED is replaced, this would imply taking baseline images for every single alignment, which is very labour intensive.

2.3.5 Epi-illumination

The addition of a 50:50 beamsplitter (Thorlabs EBS1) to the setup, placed between objective and lens at a 45° angle with respect to the optical path, allowed for epi-illumination. To test if sufficient light is still able to reach the sensor, first the continuous LED mini-light was used, which results are shown in Fig. 2.13. Still enough signal is present to make images in which the droplets' morphologies are visible, but images are becoming a bit more grainy due to the higher signal to noise ratio. It also becomes clear from the image that the field of view has become narrower, only a smaller depth of the sample is now visible and droplets that are out of focus become vague shadows in this case. In principle this shallower field of view is not a problem, but alignment needs to be more precise, which is something that has to be taken into account when the imaging setup is placed on the cDICE setup for imaging. One then needs to be able to align along axial direction in a very precise manner, to make sure that droplets appear sharp.

As the continuous light source proved the epi-illumination via a 50:50 beamsplitter to work, the pulsed high-power LED was also tried, which results are shown in Fig. 2.14. As the light yield of

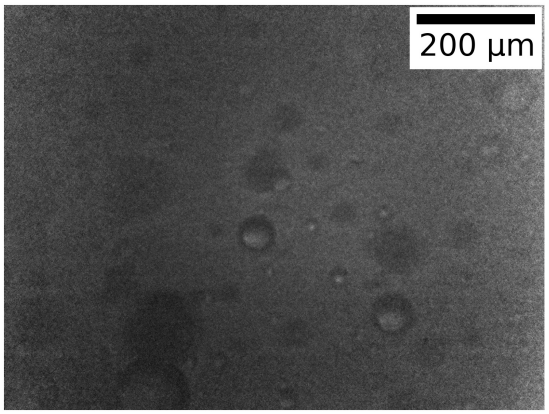

Figure 2.13: Epi-illumination with beamsplitter and continuous light source.

this pulsed illumination source is much lower in the short exposure times used (25 µs), even less signal reaches the sensor than with epi-illumination using the continuous light source, which is made clear by the absence of any visible droplets in Fig. 2.14b, where nothing was placed behind the sample (identical to the setup used for continuous epi-illumination described before). Placing a reflective mirror behind the sample improved the image significantly, as is shown in Fig. 2.14a.

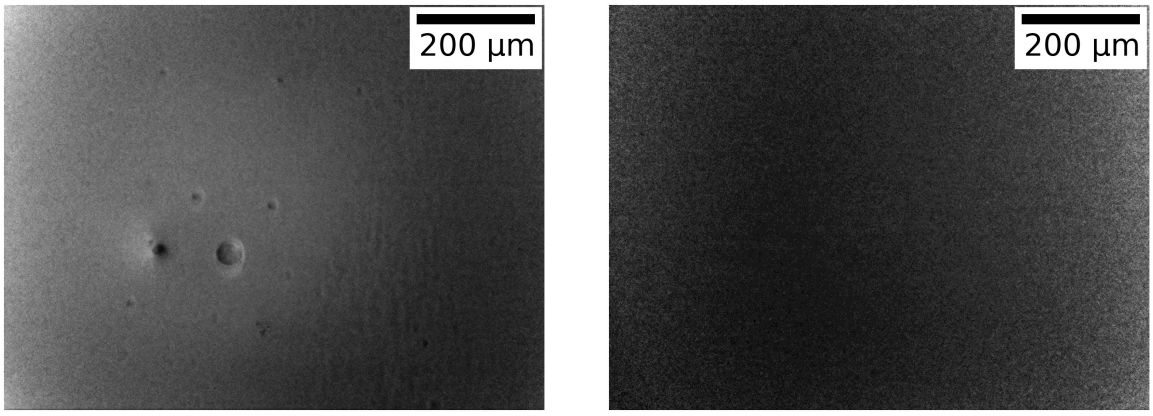

Figure 2.14: Epi-illumination with the pulsed high-power LED via beamsplitter **(a)** with and **(b)** without a mirror placed behind the sample, exposure time was in both cases set to 25 µs.

2.3.6 Model System Limitations

Despite being a useful tool to explore ideas and learn which ideas work and which do not, a model system is always limited in its representation of the real system. There are several factors that are different in the cDICE-setup compared to the model system, which can complicate the applicability of the illumination setup to the cDICE setup. First, the sample is much shallower than the cDICE chamber, giving less background signal with trans-illumination. The rotating oil the cDICE chamber will presumably give a more dynamic background signal, that is harder to average out or subtract. The illumination intensity will also be affected by the thicker layer of oil, as part of the light is absorbed, when using trans-illumination. In the current setup, the lid of the chamber is largely closed (see Fig. 1.3b), to prevent the contents from being spun out the chamber when it is rotating. This makes that illumination or imaging also need to occur through this plastic material. In theory also glass chambers could be used, and have been before, which would probably already improve on signal transmission.

Furthermore, the model system is a static system, the droplets and background were not moving.

The necessary illumination times were implied from calculations based on flow rate and the assumption that all of the encapsulation buffer is converted to droplets, which is probably not the case. In theory, illumination times in the low µs-range should be sufficient, but tests on the setup will need to show whether that assumption is indeed valid.

2.3.7 Imaging in cDICE-setup

To verify whether the imaging setup with epi-illumination is also able to image the moving droplets in the cDICE setup, the imaging setup was mounted on a standard lab stand in vertical orientation with the objective pointing downwards, as in Fig. 2.15. To allow for easy translation along the optical axis, the imaging setup was placed on a lablift

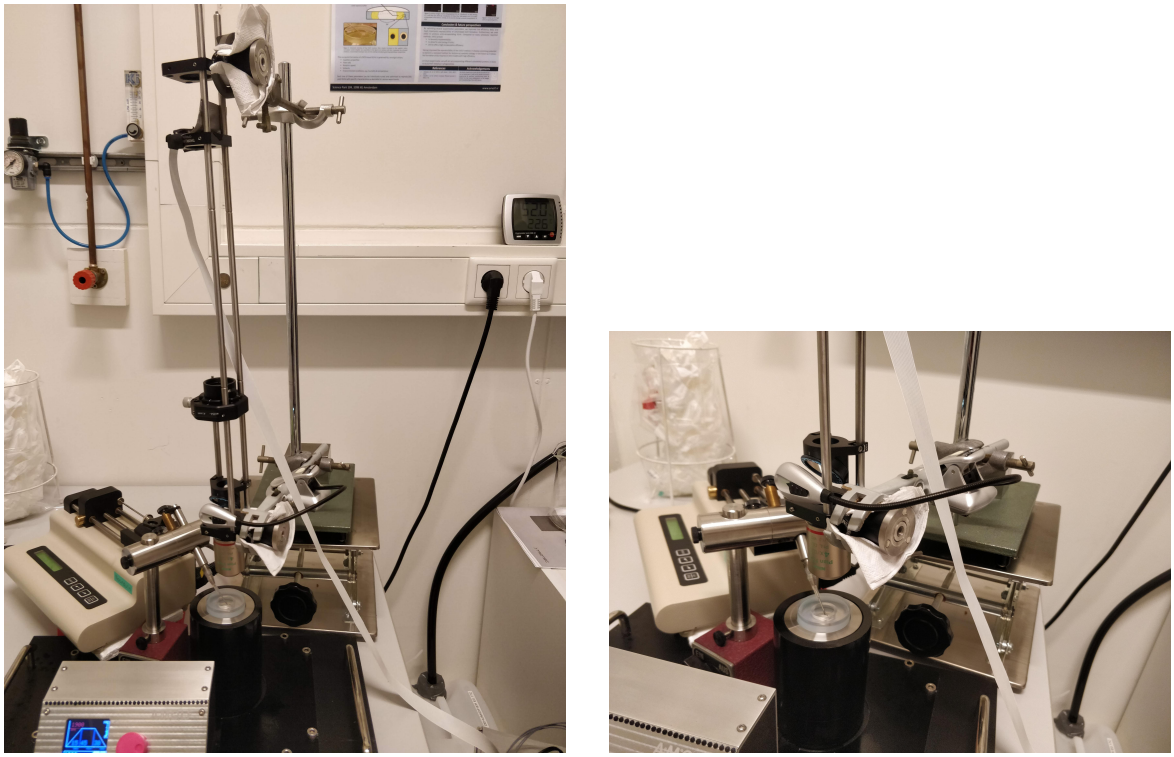

(a) (b)

Figure 2.15: Pictures of the illumination setup on the cDICE-setup with a continous light source.

Even with the lablift, several attempts to align the setup such that the capillary was visible failed. The movement in both axial and lateral direction was in this case too course, because the setup could only manually translated by moving the whole lab stand. This leads to conclude that the current imaging setup is not yet suitable for imaging on the cDICE, as lack of focus on the capillary will also result in lack of focus on the moving droplets.

2.4 Conclusions and Outlook

Although both epi- and trans-illumination are able to give reasonable images with the model system, trans-illumination gives much better images in terms of brightness and contrast. In trans-illumination, droplets are easy to distinguish from the background signal and shorter exposure times can be used for pulsed light sources to achieve the same degree of illumination as with epi-illumination. Focusing and alignment also proved to be much easier when trans-illumination is possible, due to the higher contrast than with epi-illumination. Based on these findings, it would therefore favour to further investigate in ways of incorporating trans-illumination in the cDICE-setup. A way of doing this could for example be the direction of the pulsed light through a glass fibre, which is flexible and therefore easier to implement. The light could then either be transmitted through (holes/slits in) the metal plate, or a small elevation of the chamber needs to be designed

where the fibre is guided through.

Chapter 3

Automated analysis of GUV samples with Python

3.1 Introduction

Computational image analysis is very well suited for particle tracking purposes and the field of colloids makes very often use of that [22, 23]. The most well-known particle tracking in the field of colloids was described by Crocker and Grier [24]. Several versions of this algorithm have been implemented in several programming languages, for example Python, IDL and C. The often used scientific image viewer Fiji also comes with a particle tracking plugin [25]. Most of these algorithms however focus on detecting maxima in brightness, which is a very reasonable method for detecting solid particles or particles whose appearance has been blurred by optical limits, therefore forming a diffuse spot, but it does not work well for detecting hollow features.

As we are dealing with giant unilamellar vesicles with a fluorescent lipid layer on the outside (see Section 1.3) and the lipid bilayer is the outer boundary of a vesicle, the best approach of determining the size would be determining the position of this bilayer, rather than using the fluorescently labelled encapsulated medium. Next to the fact that we want to track hollow vesicles, in the sense that the lipid channel only contains data on the membrane and not on the vesicle's interior, the vesicles can be quite polydisperse in size. Particle tracking libraries from the field of colloidal chemistry are mostly optimised towards detecting reasonably monodisperse particles, with polydispersities on the order of a few percent, which does not apply to our vesicles where one batch can easily contain vesicles between 5 μm to 50 μm in diameter.

Many groups implement their own tracking algorithm, because it gives the flexibility to be optimised for the type of data that is collected from samples [26]. Chenouard et al. already show the difficulty to objectively compare different tracking algorithms among each other, since for real image data no ground truth is available [26]. Obtaining ground truth for real image data is very hard, if not impossible at all, as manual annotation by humans is largely dependent on the observer and also very labour intensive for large datasets [26–29]. This makes is extremely difficult to exactly check the validity of tracking.

Nevertheless, as our data consists of relatively large giant unilamellar vesicles (GUVs) typically at low densities, our eyes can quite reliably verify the accuracy of tracking. The tool should therefore merely be used as assistance to the user and human input and validation will be necessary in any case. Previously, the approximate positions of the centres of GUVs were selected by hand, which is prone to errors, especially along the z-axis as it is hard to compare GUV radii between two adjacent frames. The new tool attempts to automatically detect the positions of GUVs, both in the (x, y)-plane and after linking also along the z-axis. This chapter describes the method behind the tracking software that was implemented in Python for the localisation of GUVs from 3D confocal image data.

3.1.1 Description of the Data

The data that is used for tracking consists of so called z-stacks. In a z-stack, multiple instances of the (x, y) image plane are present, that are imaged subsequently. Once the scanning of one frame by the confocal microscope is finished, the sample is moved in z direction, to scan a new image

plane. The z-stack is then basically a list, or array, of (x, y) image planes, as shown schematically in Fig. 3.1.

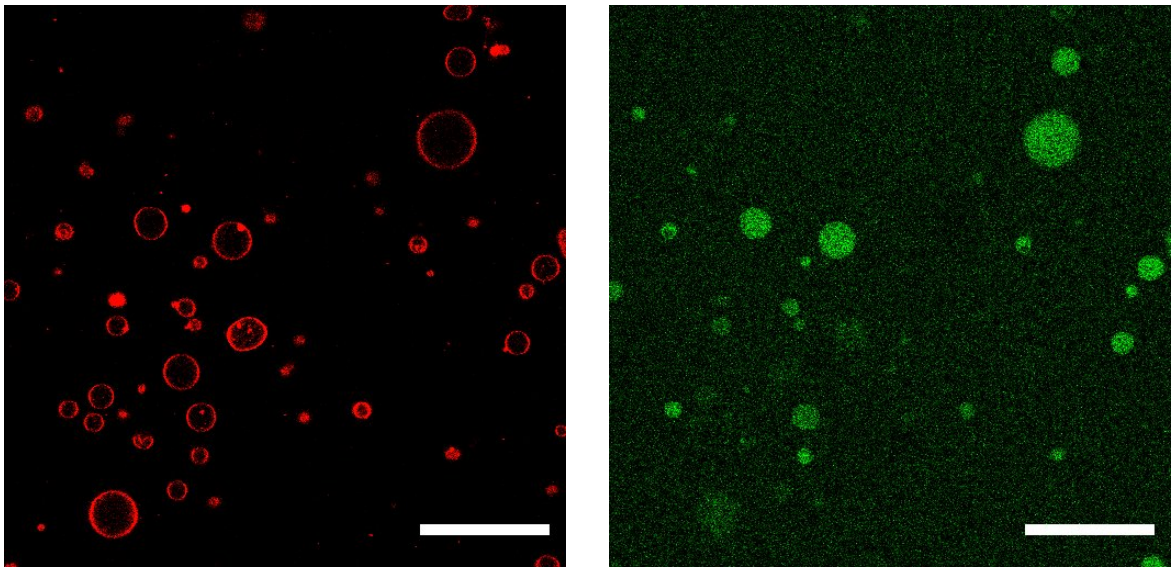

(a) (b)

Figure 3.1: Example of the two channels within a z-stack of GUVs. The red channel (**(a)**) represent the lipid membrane, while the green channel (**(b)**) is the fluorescently labelled interior.

Each of these (x, y) image planes, or "frames" for short, consists of $N \times M$ pixels, each containing a value describing the intensity of that pixel. As we are dealing with 16-bit images, these values lie between 0 and 65 535 ($= 2^{16} - 1$). When loading the image into an image viewer, generally the higher values correspond to a brighter pixel, while the lower values represent a dimmer pixel. We can view this image as a grayscale image, in which the value 0 then corresponds to a black pixel and the value 65 535 then corresponds to a completely white pixel. In the code, a frame is treated as a list of these pixel values, in the form of an $N \times M$ NumPy array [30]. A z-stack of L frames then directly corresponds to a $L \times N \times M$ array.

3.2 Methods

3.2.1 Feature Tracking

The feature tracking is applied to each frame separately. We loop over all L frames and store the found positions in a large *DataFrame* from the `pandas` Python module [31], which is comparable to an excel table where the data is stored in rows, each row corresponding to one feature, while the variable names are represented as different columns, as illustrated in Fig. 3.2.

Figure 3.2: Illustration of the structure of a *DataFrame*

x	y	r	$frame$
x_1	y_1	r_1	$frame_1$
x_2	y_2	r_2	$frame_2$
$\vdots$	$\vdots$	$\vdots$	$\vdots$
x_n	y_n	r_n	$frame_n$

The feature tracking consists of three steps:

1. Edge detection of the features using the Canny algorithm
2. Filling the holes within the edges
3. Detecting separate features

Edge Detection

For the detection of the edges of the features, the Canny edge detection algorithm was used [32]. This algorithm first uses a Gaussian blur to smoothen the image and decrease background noise. Afterwards edges are detected based on the maxima in the gradient of the intensity. This detection mechanism is very versatile and therefore applicable to both smooth and step edges. [32]

3.2.2 Hole Filling

After edge detection, the space in between of the edges could be filled using a binary hole filling function. We made use of the `binary_fill_holes` function within the `ndimage` module of the SciPy package [33]. As the vesicles are closed spheres, all spaces within the vesicles should be filled.

3.2.3 Detecting Separate Features

After the hole filling, the separated features needed to be detected. This was carried out using the `label` function of the `measure` module within the Scikit-image Python module [34]. This function labels all connected pixels with the same value into the same group, as the different features are separated by black pixels, all features will gain their own group number.

3.2.4 Feature Linking

Once features have been located in all frames, the features can be linked together, to group features that belong to the same GUV. The process is schematically illustrated in Fig. 3.3. Since the feature tracking is not perfect, it can occur that a feature is missed in a certain frame (or a multiple) along the z-direction. The algorithm therefore links all features based on two criteria: a threshold distance in the xy (in units of pixels) and a threshold distance in the z direction (in units of frames). Note that the z threshold distance could also be translated to physical units by considering the z step size, which is set at a constant value of 1 μm.

A neighbour list is built for features that satisfy both distance threshold. By looping over the neighbour list trajectories are formed based on common neighbours. For example if feature a and b are neighbours and feature b and c are also neighbours, then a, b, c are all grouped into the same trajectory.

Then trajectories are filtered, single particles are removed, since a GUV can never be present in only a single frame, due to its size and too short short trajectories are also removed for the same reason. The minimal track length can be altered as a parameter in the tracking software.

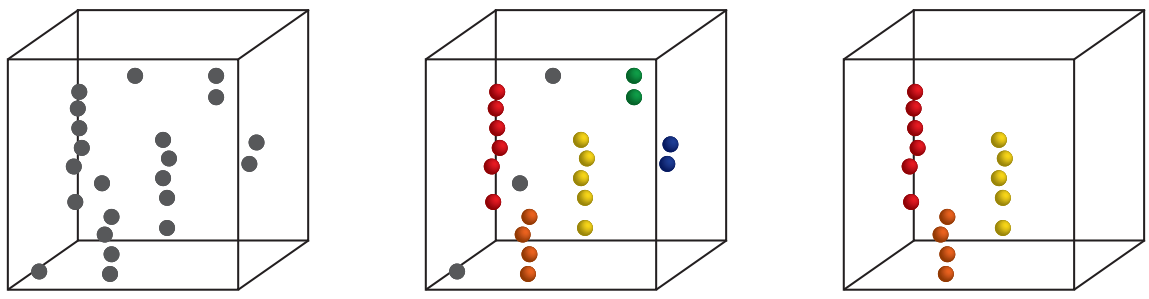

Figure 3.3: Illustration of the feature linking, **(a)** shows all tracked features. **(b)** the features that lie within threshold distance from each other are linked together into the same trajectory and **(c)** single features, or too short trajectories are removed. Different colours distinguish different trajectories.

3.2.5 Modifications by user

To make the software accountable and the results verifiable, all tracked results are displayed to the user and can be altered by the user as well. The main graphical user interface (GUI) is displayed in Fig. 3.4. On the left the adjustable parameters are shown, in the middle the most important results for determining the accuracy of tracking and on the right the confocal data with the tracking results overlaid is shown. The confocal data stack is scrollable and the user can delete falsely detected features easily by clicking it. Upon deletion of a GUV, the results are automatically updated. Once the tracking and validation by the user are done, the results can be saved to a comma separated value file with the button in the lower left corner.

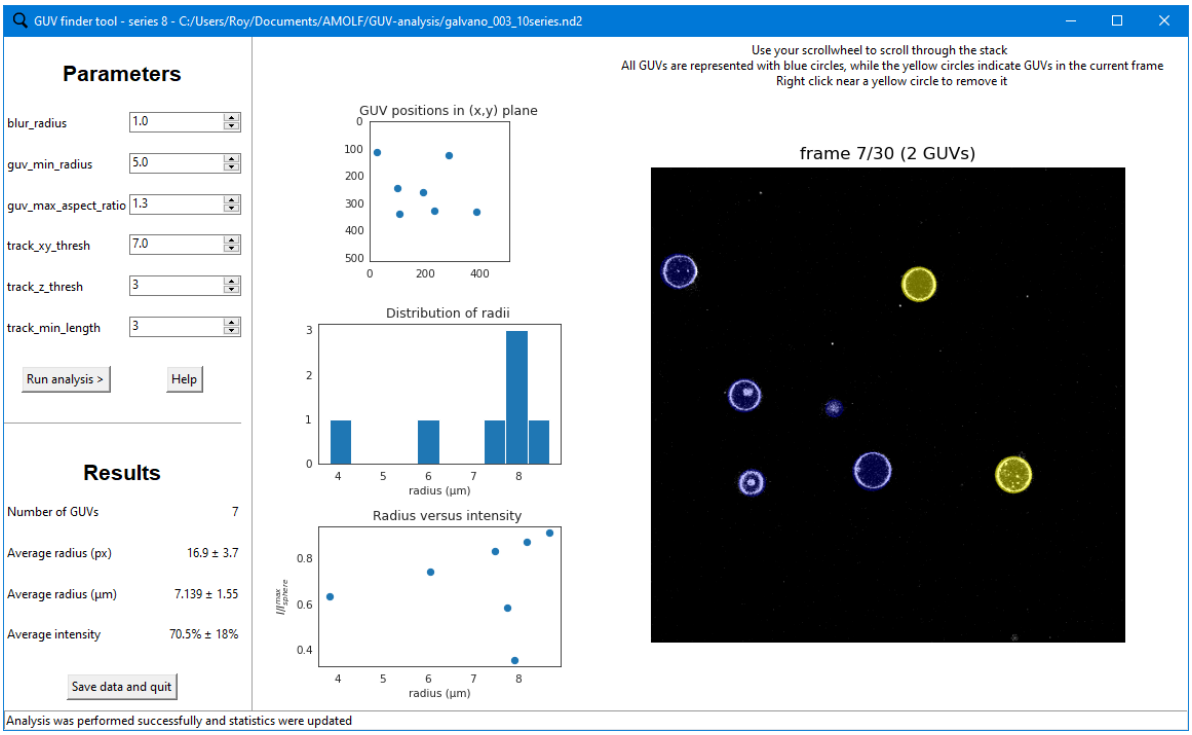

Figure 3.4: Impression of the graphical user interface of the tracking software.

3.3 Results and Discussion

The analysis software was only applied to measured confocal microscopy data, to allow us to optimise parameters for the data that we have. No simulated images were subjected to tracking, which means that no ground truth was available on the tracked positions and verification had to occur by inspection by eye. All shown images were recorded by Lori Van de Cauter on a Nikon A1R-MP multi-photon confocal microscope with a Nikon 60x Plan APO IR NA/1.27 water-immersion objective.

3.3.1 Feature Detection

As mentioned before, the edge detection was performed using the Canny algorithm. Different steps of the feature detection are displayed in Fig. 3.5. In this case a Gaussian blur with σ =1 px was applied, which is enough to discard any background noise, but still sufficiently low to prevent blurring the edges of the GUVs which would lead to overestimation of the vesicle sizes in later steps. As shown in Fig. 3.5b, the edges get detected well, both inner and outer edge of the vesicle. It also shows that the small dot inside the GUV is processed and its edges are detected as well. As we proceed with the binary hole filling, which results are shown in Fig. 3.5c, we see that the dot inside the GUV is eliminated as the whole GUV gets evenly filled.

It can also be that two GUVs are close to each other, such as shown in Fig. 3.6. If this is only the case

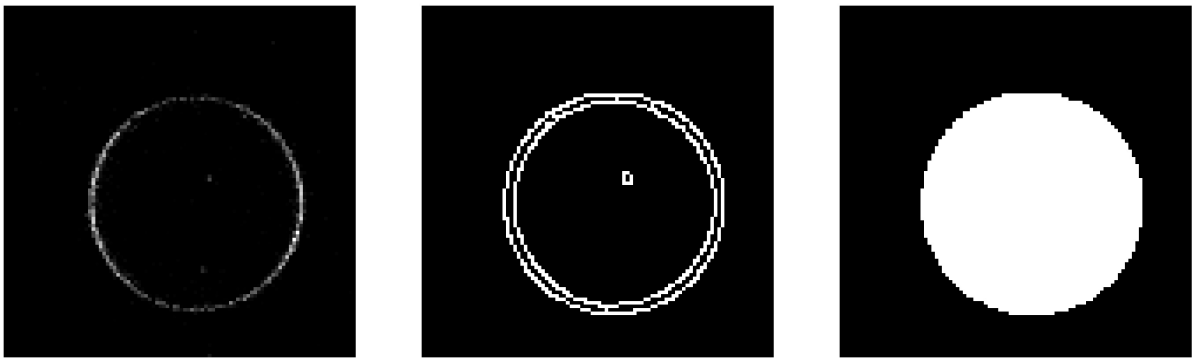

(a) (b) (c)

Figure 3.5: Different steps for feature detection, **(a)** shows the raw confocal data, **(b)** the edge detection and **(c)** the data after filling the holes between edges.

for certain frames, it does not form a direct problem for the tracking, as the radii of the GUVs differ per frame and therefore several frames higher of lower, the GUVs will most likely be separable. The top row of Fig. 3.6 shows the data at a frame in which the GUVs are too closed to be resolved individually by the algorithm, while two frames higher in z-direction (bottom row of Fig. 3.6), the GUVs are resolved individually. As the algorithm tries to detect GUVs in each frame separately before linking, two close GUVs can still be resolved individually.

3.3.2 Feature Linking

After the feature detection was applied, which is the most crucial step in the whole process since it largely influences the results, the points should be linked together along the z-direction. The feature detection results in a large data frame with all features found and their properties. This data frame is first filtered based on two criteria: a maximum aspect ratio and a minimum radius. The first is to throw out the features that contain aggregates, as sizes will not be determined properly and the latter is to obey any noise that was tracked as a feature by mistake. The neighbour list is built based on threshold distances in x, y and z and common neighbours are linked together into the same trajectory. The z-threshold is mainly to make sure that features were one frame along z is missing, for example because the GUV was too close to another point in that frame, are still linked together. All points without neighbours were discarded and a typical result is shown in Fig. 3.7a.

For each of the trajectories the feature with largest area is selected as the GUV centre, as the spherical GUV should be largest at its centre. The positions of the centres for the same dataset are shown in Fig. 3.7b. It is clear that in most cases the determined centre is indeed found in the middle of the trajectory.

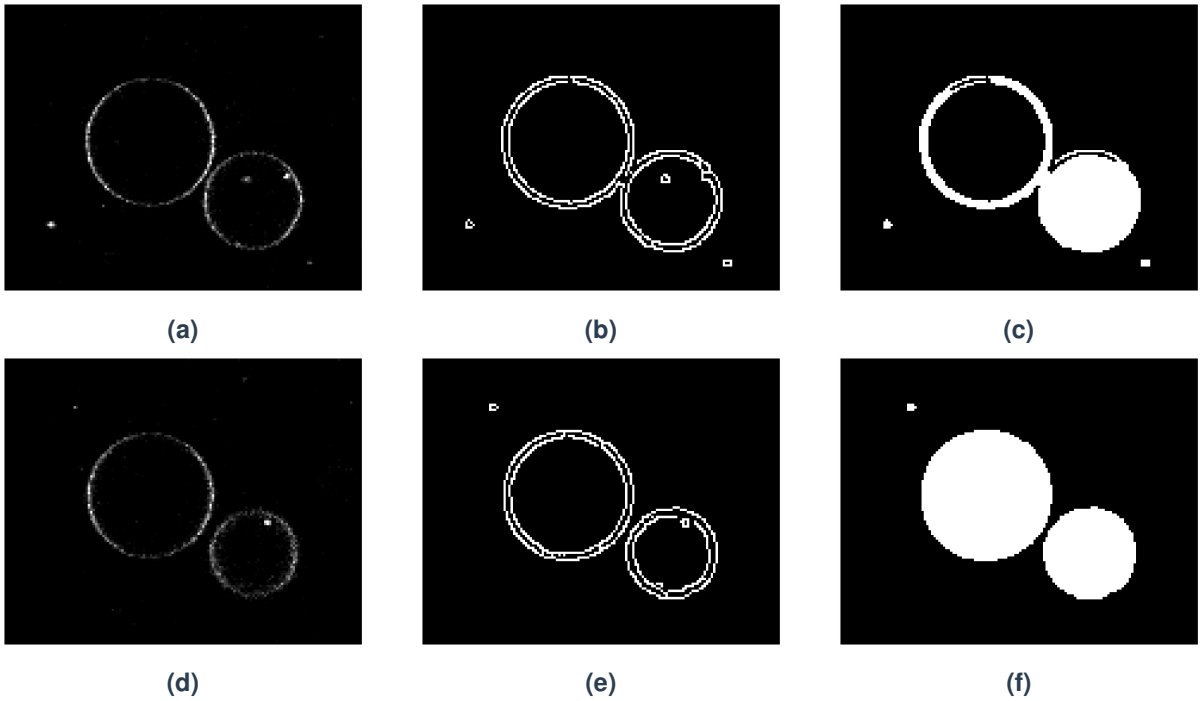

Figure 3.6: Different steps for feature detection, **(a,d)** shows the raw confocal data, **(b,e)** the edge detection and **(c,f)** the data after filling the holes between edges. The frames in the bottom row (**(d)**-**(f)**) are two frames up in z-direction, compared to the top row.

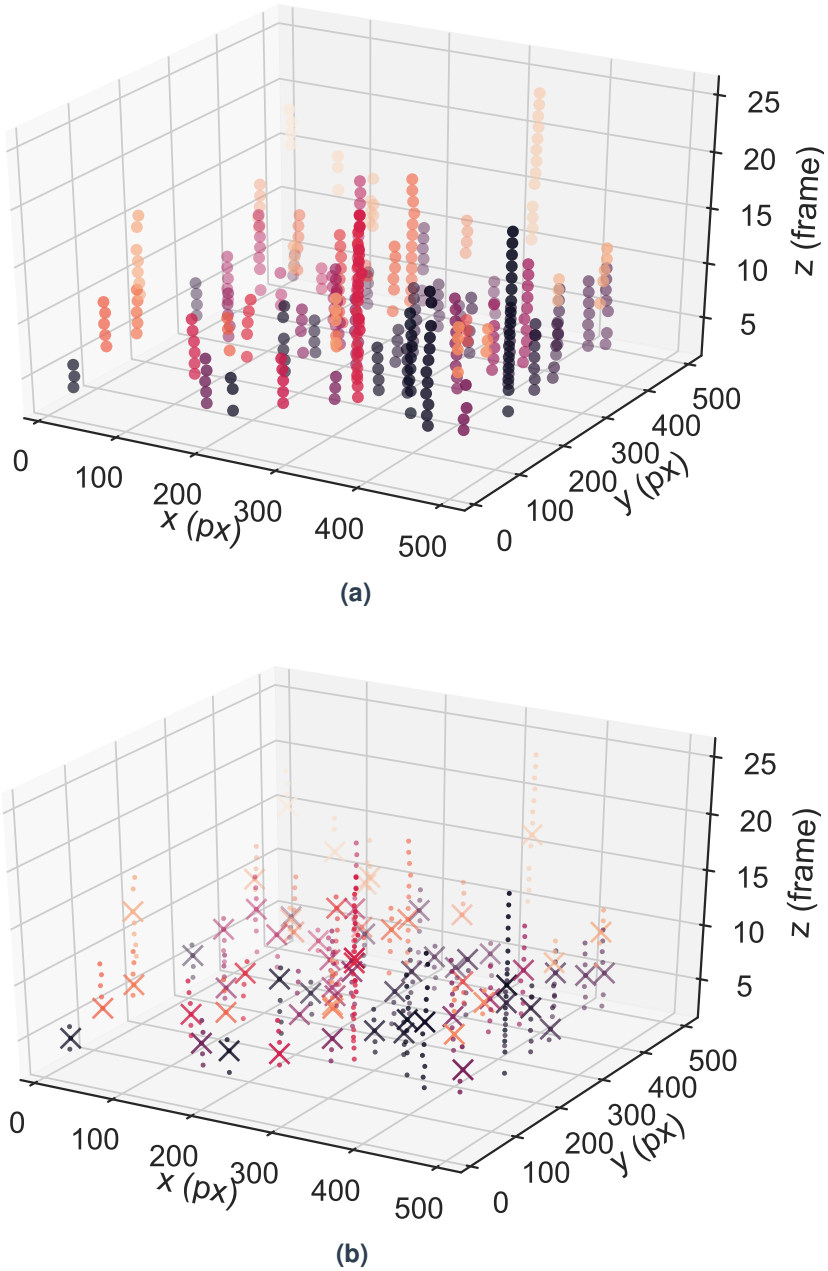

Figure 3.7: Example of the tracking result after feature linking, different trajectories are represented by different colours. In **(a)** all features are shown and in **(b)** the centres are marked with an *x*.

3.3.3 General Tracking Result

In Fig. 3.8 an example of a tracking result is shown. No manual deletion was yet applied, these images show the results as produced by the tracking software. It is clear that both small and larger GUVs are tracked accurately. As the yellow circles indicate that the shown frame is the one in which the centre of the GUV was found we can see how well the radii of the GUVs are estimated. In general, for the spherical GUVs this estimation of the radius seems accurate as the yellow circles surround the membrane area and are not larger than the GUVs. As we do not have a ground truth for these measured samples, we cannot directly make any assumptions on the accuracy of the estimation of the radii, the only way to judge the estimation is inspection by eye, from which it seems to be accurate.

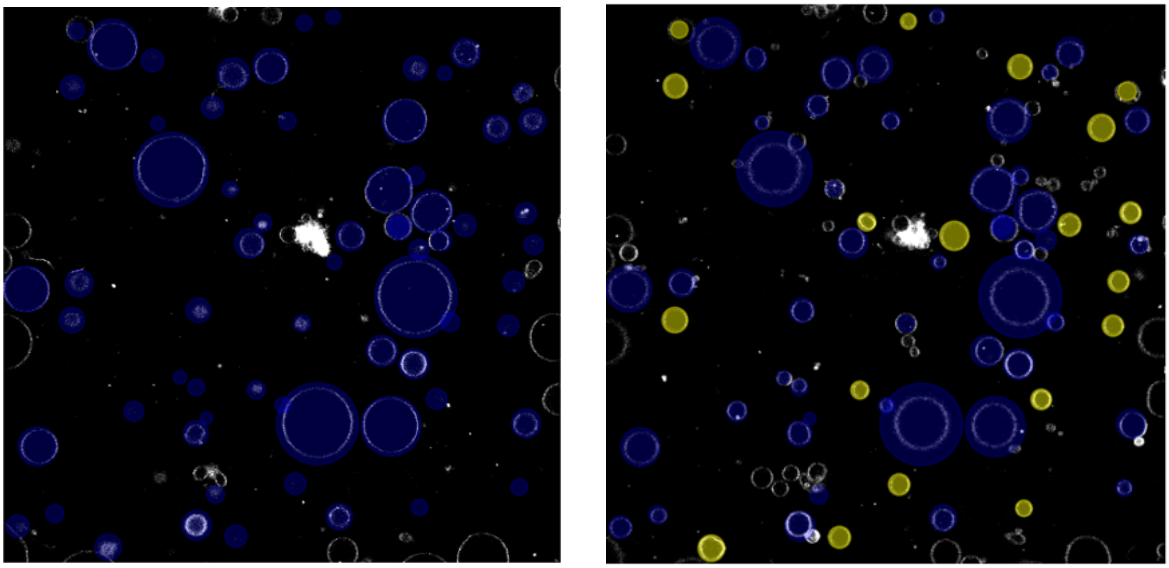

(a) (b)

Figure 3.8: Two frames from a general tracking result at different z-positions. The blue and yellow circles indicated tracked GUVs, where yellow means that the shown frame is the one in which the area was largest and is thus marked as the GUV's centre.

3.3.4 Pittfalls

Even though the software generally tracks the features well, especially with optimised parameters tuning by the user, there are a few cases in which it is not able to resolve GUVs well.

The software is optimised for spherical GUVs and therefore assumes all features are more or less spherical. Although the found features can to some extend be tuned by increasing the maximum allowed aspect ratio, for determining the GUV's radius a sphere is assumed. This was a deliberate choice, as GUVs are supposed to be spherical, when dispersed in an aqueous medium of the same osmolarity as the inner medium. Generally the longest side of an ellipsoidal GUV is considered as the radius, so the radius in these cases is overestimated, as is shown in Fig. 3.9a.

The presence of aggregates can also lead to a false detection of features, as is shown in Fig. 3.9b-c. The filtering based on aspect ratio does not allow for deletion of these false features, but they can easily be removed by the user in the software, as it is quite clear that it is not a GUV.

Both of these pittfalls occur only rarely in good samples and can easily be removed by the user upon inspection of the results of tracking.

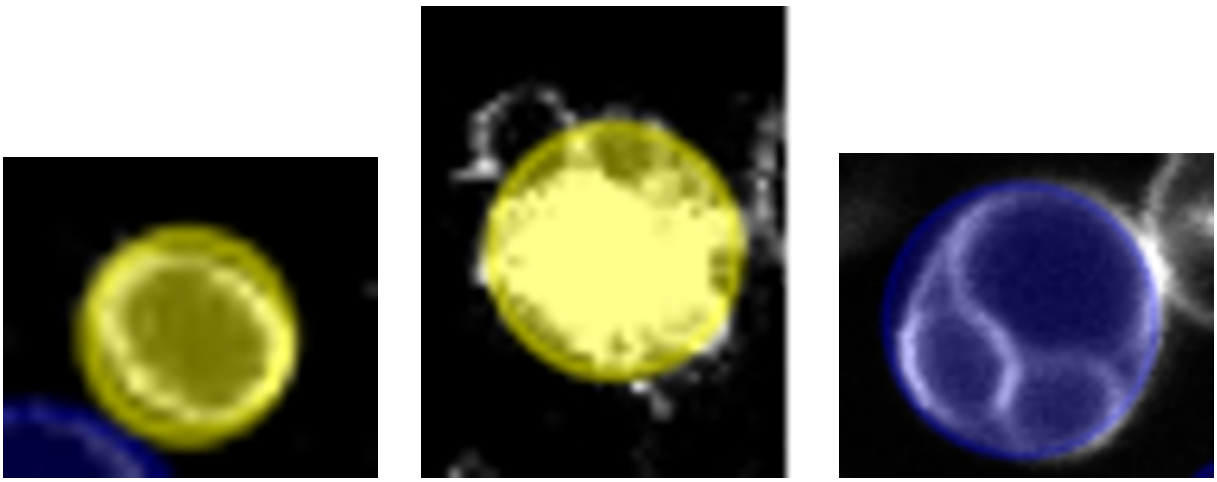

(a) (b) (c)

Figure 3.9: Examples of features that cannot be tracked accurately by the software, **(a)** displays a GUV that is not completely spherical and **(b)-(c)** show spherical aggregates that are wrongly detected as GUVs.

3.4 Conclusions

The aim of the software was to reliably detect the positions and sizes of giant unilamellar vesicles in confocal microscopy data. For low-density samples with low noise, in which all GUVs are separated well, the software is easy to detect all GUVs and accurately determine their radii. As the density increases, more aggregates will form and the software is not always able to resolve all GUVs individually. As long as the sample is not too dense, meaning most GUVs are at least separated at some distance from each other in several frames, the software will still be able to track them, but their might be a small underestimation in the radii, as there is a probability that in the frame where a GUV has the highest radius, the two neighbouring GUVs cannot be resolved. Nevertheless, most confocal data of these vesicles is of quite low density to which the software is well suited.

Chapter 4

Conclusions and Outlook

The goal of this internship was to shed light on the production of giant unilamellar vesicles, produced by the cDICE method. For this relatively new technique with large potential, still many facets of the GUV synthesis procedure and the large parameter space are unexplored.

The imaging setup, as proposed in Chapter 2, is very well able to image emulsion droplets inside a glass capillary with both continuous as well as short-exposure pulsed light sources. Epi-illumination does work but has some clear limitations: the field of view becomes narrower, implying higher precision in alignment is needed, more light is required to achieve the same image qualty as with trans-illumination, implying the need for either stronger LEDs or longer exposure times. In the cDICE-setup the maximum exposure time will be limited, as longer exposure times will lead to motion blur and therefore leads to the impossibility of determining the droplet morphologies at high speed. Trans-illumination therefore seems the method of choice, but implementation in the cDICE-setup is difficult. The current setup also does not yet allow for fine alignment when mounted onto the cDICE-setup, which makes current usage on the cDICE not yet possible.

The developed tool for analysis of the confocal datasets obtained for the GUVs has in general high accuracy in tracking the positions and sizes of the GUVs. Some minor problems arise in higher-density datasets, as aggregates will either be excluded from analysis or lead to an incorrect radius estimation. These problems can easily be solved by the user operating the software, manually deleting the wrong features. The software is therefore still able to massively speed up the process of data analysis, as most of the work is taken care off by the software, instead of the user.

Outlook

The data analysis tool is by now a ready-to-use solution that works well on most of the data that is generated. The major limitation is being only applicable to spherical vesicles, a feature that could be changed in a new version of the software. Allowing tracking of features of other shapes, allows for other data types, such a vesicles spread on a support. As each type of data has its own specifics, the parameters will always need to be adjusted for a new system.

Before the imaging setup can be used on the cDICE-setup some adjustments are necessary. Trans-illumination seems to be the illumination method of choice, since the contrast is much better and shorter exposure times are possible. The model system should first be modified, to resemble the nature of a cDICE chamber more. A chamber could then be completely filled with the model emulsion that was used, but imaging through the chamber's lid already improves resemblance to the real system. As we will be largely limited by exposure time, any gain on that is helpful. The easiest way of incorporating trans-illumination will probably be by collimating the LED light into a glass fibre and lead the fibre through the hollow base of the rotating platform. With the addition of a glass fibre, other illumination spots become also readily available, such as guiding the fibre along the capillary. One must then make sure that the fluid flow within the cDICE chamber is not distorted, to prevent unwanted side effects.

Furthermore, for alignment of the imaging setup, a translation stage would definitely be necessary. Course alignment can most certainly be performed by hand, but a translation stage can then be used for the fine alignment, which will be necessary for the shallow field of view of the setup.

Bibliography

[1] Möller, J.; Lühmann, T.; Chabria, M.; Hall, H.; Vogel, V. Macrophages lift off surface-bound bacteria using a filopodium-lamellipodium hook-and-shovel mechanism. *Scientific Reports* **2013**, *3*, 2884.

[2] Ganzinger, K. A.; Schwille, P. More from less – bottom-up reconstitution of cell biology. *Journal of Cell Science* **2019**, *132*, jcs227488.

[3] Alberts, B.; Johnson, A.; Lewis, J.; Morgan, D.; Raff, M.; Roberts, K.; Walter, P. *Molecular Biology of the Cell*; Garland Science: New York, 2015; pp 1–41.

[4] Fenz, S. F.; Sengupta, K. Giant vesicles as cell models. *Integrative Biology* **2012**, *4*, 982.

[5] Göpfrich, K.; Platzman, I.; Spatz, J. P. Mastering Complexity: Towards Bottom-up Construction of Multifunctional Eukaryotic Synthetic Cells. *Trends in Biotechnology* **2018**, *36*, 938–951.

[6] Lagny, T. J.; Bassereau, P. Bioinspired membrane-based systems for a physical approach of cell organization and dynamics: usefulness and limitations. *Interface Focus* **2015**, *5*, 20150038.

[7] Walde, P.; Cosentino, K.; Engel, H.; Stano, P. Giant Vesicles: Preparations and Applications. *ChemBioChem* **2010**, *11*, 848–865.

[8] Reeves, J. P.; Dowben, R. M. Formation and properties of thin-walled phospholipid vesicles. *Journal of Cellular Physiology* **1969**, *73*, 49–60.

[9] Angelova, M.; Dimitrov, D. S. *Trends in Colloid and Interface Science II*; Steinkopff: Darmstadt, 2007; Vol. 67; pp 59–67.

[10] Angelova, M. I.; Dimitrov, D. S. Liposome electroformation. *Faraday Discussions of the Chemical Society* **1986**, *81*, 303.

[11] Abkarian, M.; Loiseau, E.; Massiera, G. Continuous droplet interface crossing encapsulation (cDICE) for high throughput monodisperse vesicle design. *Soft Matter* **2011**, *7*, 4610.

[12] Dimova, R. Giant Vesicles and Their Use in Assays for Assessing Membrane Phase State, Curvature, Mechanics, and Electrical Properties. *Annual Review of Biophysics* **2019**, *48*, 93–119.

[13] Jonkman, J.; Brown, C. M.; Wright, G. D.; Anderson, K. I.; North, A. J. Tutorial: guidance for quantitative confocal microscopy. *Nature Protocols* **2020**, *15*.

[14] Prasad, V.; Semwogerere, D.; Weeks, E. R. Confocal microscopy of colloids. *Journal of Physics: Condensed Matter* **2007**, *19*, 113102.

[15] Curry, A.; Wax, A. Epi-illumination darkfield through a microscope objective for imaging and spectral analysis of nanoparticle interaction with cells in culture. Biomedical Optics. Washington, D.C., 2006; p SF7.

[16] Versluis, M. High-speed imaging in fluids. *Experiments in Fluids* **2013**, *54*, 1458.

[17] van der Bos, A.; Zijlstra, A.; Gelderblom, E.; Versluis, M. iLIF: illumination by Laser-Induced Fluorescence for single flash imaging on a nanoseconds timescale. *Experiments in Fluids* **2011**, *51*, 1283–1289.

[18] Juhasz, T.; Kastis, G. A.; Suárez, C.; Bor, Z.; Bron, W. E. Time-resolved observations of shock waves and cavitation bubbles generated by femtosecond laser pulses in corneal tissue and water. *Lasers in Surgery and Medicine* **1996**, *19*, 23–31.

[19] Vasil'ev, R. V.; Lubsandorzhiev, B. K.; Pokhil, P. G. A nanosecond light source for scintillation- and Cerenkov-detector calibration. *Instruments and Experimental Techniques* **2000**, *43*, 570–572.

[20] Raspberry Pi Foundation, Camera Module. 2020; https://www.raspberrypi.org/documentation/hardware/camera/.

[21] Sneha, H. Pixel Intensity Histogram Characteristics: Basics of Image Processing and Machine Vision. 2017; https://www.allaboutcircuits.com/technical-articles/image-histogram-characteristics-machine-learning-image-processing.

[22] Imhof, A.; Blaaderen, A. V. Switching plastic crystals of colloidal rods with electric fields. **2014**, 1–8.

[23] Salipante, P. F.; Hudson, S. D. A colloid model system for interfacial sorption kinetics. *Langmuir* **2015**, *31*, 3368–3376.

[24] Crocker, J. C.; Grier, D. G. Methods of Digital Video Microscopy for Colloidal Studies. *Journal of Colloid and Interface Science* **1996**, *179*, 298–310.

[25] Schindelin, J. et al. Fiji: an open-source platform for biological-image analysis. *Nature Methods* **2012**, *9*, 676–682.

[26] Chenouard, N. et al. Objective comparison of particle tracking methods. *Nature Methods* **2014**, *11*, 281–289.

[27] Smal, I.; Draegestein, K.; Galjart, N.; Niessen, W.; Meijering, E. Particle Filtering for Multiple Object Tracking in Dynamic Fluorescence Microscopy Images: Application to Microtubule Growth Analysis. *IEEE Transactions on Medical Imaging* **2008**, *27*, 789–804.

[28] Dorn, J. F.; Danuser, G.; Yang, G. *Methods in Cell Biology*; 2008; Vol. 85; pp 497–538.

[29] Huth, J.; Buchholz, M.; Kraus, J. M.; Schmucker, M.; von Wichert, G.; Krndija, D.; Seufferlein, T.; Gress, T. M.; Kestler, H. A. Significantly improved precision of cell migration analysis in time-lapse video microscopy through use of a fully automated tracking system. *BMC Cell Biology* **2010**, *11*, 24.

[30] van der Walt, S.; Colbert, S. C.; Varoquaux, G. The NumPy Array: A Structure for Efficient Numerical Computation. *Computing in Science & Engineering* **2011**, *13*, 22–30.

[31] Reback, J. et al. Pandas 1.0.3. 2020; https://doi.org/10.5281/zenodo.3715232.

[32] Canny, J. A Computational Approach to Edge Detection. *IEEE Transactions on Pattern Analysis and Machine Intelligence* **1986**, *PAMI-8*, 679–698.

[33] Virtanen, P. et al. SciPy 1.0: fundamental algorithms for scientific computing in Python. *Nature Methods* **2020**, *17*, 261–272.

[34] van der Walt, S.; Schönberger, J. L.; Nunez-Iglesias, J.; Boulogne, F.; Warner, J. D.; Yager, N.; Gouillart, E.; Yu, T. scikit-image: image processing in Python. *PeerJ* **2014**, *2*, e453.

Chapter 5

Acknowledgements

This internship is by far the most collaborative project I have encountered in my studies so far and I noticed I really liked collaborating with other people that each have their own specific knowledge and skills. It is quite special that we all managed to make this collaborative project work, considering I had to work on most of the project from home, due to the COVID-19 pandemic. I first want to thank everyone in the Physics of Cellular Interactions group for welcoming me for my internship and discussing both science and non-science related topics every week during our group meetings and frequent coffee breaks. In particular I would like to thank Kristina for giving me the opportunity to do this project, being it very different from what we had initially in mind, but considering all circumstances, I think we made it into a worthy alternative. Furthermore I would like to thank Lori and Chris for their help with my experiments and all other members of the group for their useful input.

The camera part of the project would most certainly not have been possible without expertise from Bob from Electronics Engineering and Ricardo from Mechanical Engineering. Thanks to both of you for your ideas and thinking along with the project. I also owe a thank you to Marko, who I bothered several times with questions about alignment, microrulers and other optical setup questions.

Michael Heymann from the University of Stuttgart has taken a large part in remodelling the project into a corona-proof project. It is sad that we could not continue with the design of the mixing nozzle, as I would have really like to spend some time in your lab working on that. Nevertheless, this project turned out very well. Thanks Micha for the input and ideas on this!

I would also like to thank Gerhard Blab for being my supervisor from Utrecht University. Thank you for checking up with me several times and useful feedback on my presentation, I am looking forward to catch up with you at the coffee breaks in the Ornstein again (if restrictions allow us to).

Last but not least, I would like to thank everyone at AMOLF for welcoming me during my internship. Although I spent much less time than I anticipated at the start of my project in March, I still felt very welcome!